Bicarbonate-controlled reduction of oxygen by the Q_A semiquinone in Photosystem II in membranes

Andrea Fantuzzi[a,1] , Friederike Allgöwer[b] , Holly Baker[a] , Gemma McGuire[a], Wee Kii Teh[a] , Ana P. Gamiz-Hernandez[b,c] , Ville R. I. Kaila[b,c,1] , and A. William Rutherford[a,1]

[a]Department of Life Sciences, Imperial College London, London SW7 2AZ, United Kingdom; [b]The Arrhenius Laboratories for Natural Sciences, Department of Biochemistry and Biophysics, Stockholm University, SE-106 91 Stockholm, Sweden; and [c]Department of Chemistry, Technische Universität München, D-85747 Garching, Germany

Photosystem II (PSII), the water/plastoquinone photo-oxidoreductase, plays a key energy input role in the biosphere. $Q_A^{\bullet-}$, the reduced semiquinone form of the nonexchangeable quinone, is often considered capable of a side reaction with O_2, forming superoxide, but this reaction has not yet been demonstrated experimentally. Here, using chlorophyll fluorescence in plant PSII membranes, we show that O_2 does oxidize $Q_A^{\bullet-}$ at physiological O_2 concentrations with a $t_{1/2}$ of 10 s. Superoxide is formed stoichiometrically, and the reaction kinetics are controlled by the accessibility of O_2 to a binding site near $Q_A^{\bullet-}$, with an apparent dissociation constant of 70 ± 20 μM. Unexpectedly, $Q_A^{\bullet-}$ could only reduce O_2 when bicarbonate was absent from its binding site on the nonheme iron (Fe^{2+}) and the addition of bicarbonate or formate blocked the O_2-dependant decay of $Q_A^{\bullet-}$. These results, together with molecular dynamics simulations and hybrid quantum mechanics/molecular mechanics calculations, indicate that electron transfer from $Q_A^{\bullet-}$ to O_2 occurs when the O_2 is bound to the empty bicarbonate site on Fe^{2+}. A protective role for bicarbonate in PSII was recently reported, involving long-lived $Q_A^{\bullet-}$ triggering bicarbonate dissociation from Fe^{2+} [Brinkert et al., Proc. Natl. Acad. Sci. U.S.A. 113, 12144–12149 (2016)]. The present findings extend this mechanism by showing that bicarbonate release allows O_2 to bind to Fe^{2+} and to oxidize $Q_A^{\bullet-}$. This could be beneficial by oxidizing $Q_A^{\bullet-}$ and by producing superoxide, a chemical signal for the overreduced state of the electron transfer chain.

photosynthesis | photoinhibition | redox signaling | photoregulation | reactive oxygen species

Photosystem II (PSII) is the water/plastoquinone photo-oxidoreductase that uses the energy of red light to drive the oxidation of water and the reduction of plastoquinone (PQ). This process leads to the formation of a radical pair on the chlorophyll $P_{D1}^{\bullet+}$ and pheophytin $Pheo_{D1}^{\bullet-}$. The electron hole is transferred from the chlorophyll cation radical, $P_{D1}^{\bullet+}$, via a redox-active tyrosine (Tyr_Z) to the Mn_4O_5Ca cluster, where, after four sequential photochemical turnovers, two water molecules are oxidized on the luminal side of the membrane. The electron is transferred from the pheophytin anion radical ($Pheo_{D1}^{\bullet-}$) via a nonexchangeable plastoquinone (Q_A), which acts as a one-electron relay, to an exchangeable plastoquinone (Q_B), the terminal electron acceptor (1–3). Q_B accepts two electrons and takes up two protons from the aqueous phase to form Q_BH_2 before it is released as a PQH_2 into the PQ/PQH_2 pool in the membrane (4). From here, the PQH_2 delivers electrons to cytochrome b_6f complex, the subsequent enzyme of the photosynthetic electron transfer chain.

As photochemical charge separation is intrinsically a one-photon-per-electron process, two photochemical turnovers are required to form PQH_2, with the one-electron reduced semiquinone, $Q_B^{\bullet-}$ formed as an intermediate. Semiquinones can be very reactive, but $Q_B^{\bullet-}$ is rendered thermodynamically stable by the environment provided by its binding site on the D1 protein (4). The electron on $Q_B^{\bullet-}$ is still able to back-react via

$Q_A^{\bullet-}$ with the S_2 and S_3 states, the two semistable intermediates of the water oxidizing enzyme (5). This back-reaction occurs by thermal repopulation of the intermediate radical pairs between $S_{2/3}Q_B^{\bullet-}$ and $P_{D1}^{\bullet+}Pheo_{D1}^{\bullet-}$. $P_{D1}^{\bullet+}Pheo_{D1}^{\bullet-}$ can either repopulate P^*, which can decay radiatively (5, 6), or it undergoes direct charge recombination, forming the chlorophyll triplet state, $^3P_{680}$ (7–9). As expected for a long-lived chlorophyll triplet state, it reacts with dioxygen to form a highly reactive singlet oxygen species, $^1O_2$, which causes photodamage (10, 11).

On the electron acceptor-side of PSII (Fig. 1), the reduced forms of the electron transfer cofactors can potentially reduce oxygen, forming superoxide radical ($O_2^{\bullet-}$) by a one-electron transfer to O_2. This would be a wasteful leak of electrons, and the $O_2^{\bullet-}$ formed could be damaging and act as redox signal within the cell. During forward electron transfer, $Q_A^{\bullet-}$ has a half-time of ∼1 ms (1) and is unlikely to react with O_2. However, when, for example, Q_B and the PQ pool are reduced, $Q_A^{\bullet-}$ is longer lived, and it is then more likely to reduce oxygen. Oxygen reduction by $Q_A^{\bullet-}$ is often discussed in the literature (12–16), but clear experimental evidence for this reaction has not been reported. Here, using PSII membranes, we have directly tested for electron transfer from Q_A^- to O_2 and for formation of superoxide. We show the reaction does occur, and we characterized the reaction in terms of the O_2 binding site using biochemical and computational

Significance

In Photosystem II (PSII), O_2 reduction by $Q_A^{\bullet-}$ is often discussed but has not been demonstrated. Here, we show in PSII membranes that $Q_A^{\bullet-}$ can reduce O_2 to superoxide, but only when bicarbonate is absent from its binding site on the nonheme Fe^{2+}. Bicarbonate's role in PSII was recently shown to involve a regulatory/protective redox-tuning mechanism linking PSII function to CO_2 concentration. A key aspect is the presence of stable $Q_A^{\bullet-}$ causing release of bicarbonate from its site on Fe^{2+}. Here, we show that under these conditions, O_2 binds to the empty site on the Fe^{2+} and is reduced by $Q_A^{\bullet-}$. This unexpected reaction may be a further indication of cross-talk between the regulation of PSII and CO_2 fixation.
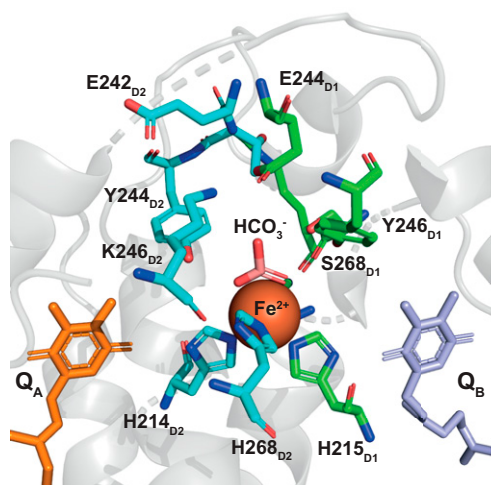
Fig. 1. The quinone-iron complex in PSII. The nonheme iron shown as a red sphere and the bicarbonate in pink. The amino acid side chains involved in the hydrogen-bonding network are shown, green if belonging to D1 and cyan if belonging to D2. Data from the 1.9-Å crystal structure (PDB ID: 3WU2) (41).

approaches. The results indicate the reaction constitutes an unexpected regulatory mechanism involving bicarbonate.

Results

$Q_A^{\bullet-}$ Oxidation by O_2. Fig. 2*A* (orange trace) shows the stability of $Q_A^{\bullet-}$ generated in low-PQ PSII membranes (*SI Appendix*, Fig. S1) under anaerobic conditions and with the concentration of $Q_A^{\bullet-}$ monitored using chlorophyll fluorescence (17, 18). To generate this state, a dark-adapted sample was illuminated with three saturating flashes in the presence of the exogenous electron donor, NH_2OH, at 250 μM, a concentration that was sufficient to donate electrons to the Mn cluster but low enough to avoid overreduction and loss of the Mn cluster in the majority of centers (*SI Appendix, Materials and Methods*, and, for example, ref. 19). This treatment resulted in the trapping of stable $Q_A^{\bullet-}$ in ~50% of the centers, based on a comparison to maximum fluorescence. The decay of $Q_A^{\bullet-}$ in the other centers is mainly due to 1) forward electron transfer in the millisecond timescale (18) as a result of the incomplete removal of the PQ pool and 2) charge recombination ($S_2Q_A^{\bullet-}$ and $S_3Q_A^{\bullet-}$) in the seconds timescale (20) in centers where electron donation from NH_2OH was insufficient to eliminate these back reactions. In the absence of O_2, the stable fluorescence signal from $Q_A^{\bullet-}$ showed a slow decay with a half-time of ~600 s. A decay rate for $Q_A^{\bullet-}$ with similar kinetics has previously been correlated with the decay of $Tyr_D\bullet$ and attributed to charge recombination between these two states (21), which could explain the slow decay of $Q_A^{\bullet-}$ observed here.

The decay of the trapped $Q_A^{\bullet-}$ state was significantly accelerated when O_2 was added back to the medium (Fig. 2*A*), which provided clear experimental evidence for the reduction of O_2 by $Q_A^{\bullet-}$. Fig. 2*A* also shows that the rate of $Q_A^{\bullet-}$ oxidation accelerated as the O_2 concentration increased. The observed fluorescence decays were found to be biphasic, with a fast exponential decay rate that depended on the O_2 concentration and a slow decay rate that was independent of the O_2 concentration. The slower phase corresponded to that observed in the absence of oxygen. The kinetic data were fitted using a linear combination of the fast exponential phase and a slow, linear decay,

$$f = e^{(k_{obs} t)} + ((b \times t) + c) \qquad [1]$$

where k_{obs} is the pseudo first-order rate constant for $Q_A^{\bullet-}$ reoxidation at a fixed O_2 concentration, b is the slope, and c is the

intercept of the linear decay observed in the absence of O_2. This biphasic behavior indicated heterogeneity in the preparation, where most of the centers were susceptible to reactions with O_2, but a smaller fraction remained unreactive. We demonstrate in the following that this heterogeneity appears to be related to bicarbonate binding to the nonheme iron. We investigated whether the effect of "connectivity" influenced the kinetics observed here in Fig. 2. Connectivity is a phenomenon seen in fluorescence when PSII shares an extended antenna, leading to a situation where there is a significant probability that excitation energy can visit more than one closed center before finding an open PSII. This results in a nonlinear relationship between fluorescence intensity and $Q_A^{\bullet-}$ concentration (22, 23). We found that connectivity has a negligible effect on the present experiment (*SI Appendix*, Fig. S2).

Fig. 2*B* shows the observed rate constants (k_{obs}) for the fast, exponential phase of the $Q_A^{\bullet-}$ decay, measured in pseudo first-order conditions and plotted as a function of the added concentration of O_2. The plot shows saturation behavior characteristic of the presence of a discrete binding site. This binding site becomes saturated above ~150 μM O_2 (*SI Appendix*, Fig. S3). The data were fitted with a hyperbolic curve (Eq. **2**) from which the apparent K_d was calculated to be 70 ± 20 μM and a rate constant, at physiological O_2 concentrations, to be 0.07 s^{-1}, corresponding to a half-time of ~10 s (10.6 ± 0.8 s). The pseudo first-order rate constant k_{obs} for $Q_A^{\bullet-}$ reoxidation at a fixed oxygen concentration was estimated as
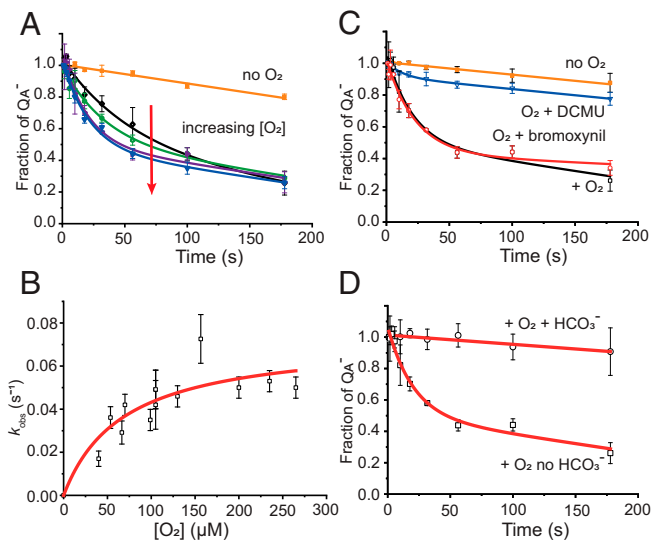

Fig. 2. Kinetics of $Q_A^{\bullet-}$ reoxidation by O_2. Fraction of $Q_A^{\bullet-}$ obtained after three saturating flashes of a degassed sample of PSII membrane fragments (60 nM PSII cores) in the presence of 250 μM hydroxylamine in a 40 mM MES buffer, 5 mM MgCl, pH 6.5. The data in *A*, *C*, and *D* were fitted to Eq. **1**. (*A*) Orange symbols represent the decay in the absence of added oxygen, and the data were fitted with a linear decay. Other symbols represent the decay in the presence of oxygen in the concentration range from 40 ± 3 μM (black symbols) to 155 ± 6 μM (blue symbols). Data were fitted with Eq. **1**. (*B*) Observed kinetic rate constants obtained from the fitting of the kinetic data with Eq. **1** plotted in function of the concentration of added oxygen. Data were fitted with the hyperbole of Eq. **2**. (*C*) Effect of the addition of Q_B site inhibitors. Control experiments with (open black symbols) and without (closed orange symbols) oxygen are shown for comparison; 10 μM DCMU (open blue symbols) or 100 μM bromoxynil (open red symbols) was added prior to the degassing step and the kinetics were measured upon the addition of 110 ± 5 μM oxygen. (*D*) Effect of the addition of 1 mM bicarbonate (open circles) at the degassing step prior to the addition of oxygen is compared with a control kinetics in the absence of bicarbonate (open squares). Kinetics were recorded upon addition of 110 ± 5 μM oxygen.

Fantuzzi et al.
Bicarbonate-controlled reduction of oxygen by the Q_A semiquinone
in Photosystem II in membranes

$$k_{\text{obs}} = \frac{k_{\text{sat}}}{(K_d^{\text{app}} + [O_2])} \qquad [2]$$

where k_{sat} is the rate constant when the binding site is fully occupied, and K_d^{app} is the apparent dissociation constant. The second-order rate constant, calculated from the linear fit, was found to be 340 ± 83 M^{-1} s^{-1}.

Influence of Herbicides on the Reactivity to Oxygen. To test if the driving force determines the rate of the electron transfer, kinetics was measured by modulating the reduction potential of $Q_A/Q_A^{\bullet-}$ by binding herbicides into the Q_B site.

Different classes of herbicides shift the potential in different directions: by $+50$ mV (-144 mV to -94 mV) with 3-(3,4-dichlorophenyl)-1,1-dimethylurea (DCMU), and by -50 mV (-144 mV to -194 mV) with bromoxynil (24). These herbicide-induced shifts in the $Q_A/Q_A^{\bullet-}$ E$_m$ result in differential effects on the kinetics of Tyr$_D^{\bullet}Q_A^{\bullet-}$ recombination (*SI Appendix*, Fig. S4), thereby confirming herbicide binding under our experimental conditions. Fig. 2*C* shows the kinetics of $Q_A^{\bullet-}$ reoxidation at 110 ± 5 μM O_2 concentration. With DCMU, the reaction was essentially blocked, whereas with bromoxynil, the reaction was virtually unaffected. Similar behavior was observed when the experiment was performed at lower O_2 concentration (40 ± 3 μM) (*SI Appendix*, Fig. S5). The effect of DCMU appears to be too drastic to be due to the small change in the $Q_A/Q_A^{\bullet-}$ reduction potential, and it is thus attributed to a structural effect of DCMU binding rather than a redox effect on the quinone (in the following, we discuss DCMU binding having a redox effect on the non-heme iron and on the binding of bicarbonate as viable options to explain its effect). The lack of a bromoxynil effect, on the other hand, suggests that the rate of O_2 reduction by $Q_A^{\bullet-}$ is not determined by the thermodynamic driving force between $Q_A/Q_A^{\bullet-}$ and $O_2/O_2^{\bullet}$. As bromoxynil occupies the Q_B site (bromoxynil binding data on flash 1 is provided in *SI Appendix*, Fig. S6*B*), this result eliminates the possibility that $Q_B^{\bullet-}$ or Q_BH_2 donates electrons to O_2, allowing the $Q_A^{\bullet-}$ to decay by forward electron transfer.

Influence of Bicarbonate on $Q_A^{\bullet-}$ Reoxidation Kinetics. The degassing used to make the PSII anaerobic is also expected to remove CO_2 and, at this pH (pH 6.5), bicarbonate from solution. The degassing is thus expected to result in partial loss of bicarbonate from PSII. Fig. 2*D* shows that addition of bicarbonate after degassing the sample, eliminated electron transfer from $Q_A^{\bullet-}$ to O_2. A control experiment using 1 mM NaCl instead of NaHCO$_3^-$ had no effect on the kinetics of $Q_A^{\bullet-}$ oxidation by O_2 (*SI Appendix*, Fig. S7*A*). Addition of bicarbonate also blocked $Q_A^{\bullet-}$ reoxidation by O_2 in the presence of the herbicides (Fig. 2*B* and *SI Appendix*, Fig. S8).

Fig. 2*D* thus suggests that bicarbonate binding to the non-heme Fe^{2+} controls electron transfer from $Q_A^{\bullet-}$ to O_2. To test the specificity of this effect, sodium formate, which is known to bind in the bicarbonate site on the nonheme Fe^{2+}, was added (*SI Appendix*, Fig. S7*B*). Formate, at 100 mM, a concentration known to be competitive with bicarbonate (25, 26), behaved like bicarbonate: it prevented $Q_A^{\bullet-}$ from reducing O_2 (*SI Appendix*, Fig. S7*B*). Because the effect is not specific to bicarbonate, this suggests electron transfer from $Q_A^{\bullet-}$ to O_2 requires that nonheme Fe^{2+} lacks the carboxylic acid and thus that the O_2 is reduced when bound to the Fe^{2+}.

Superoxide as the Product of the Reaction. The electron paramagnetic resonance (EPR) spin trap 5-(diisopropoxyphosphoryl)-5-methyl-1-pyrroline-N-oxide (DIPPMPO) was used to demonstrate $O_2^{\bullet-}$ formation under continuous illumination (Fig. 3*A*). This spin trap forms trapped radical adducts with either $O_2^{\bullet-}$ or the more reactive OH$^{\bullet}$, but these can be distinguished by their different EPR spectra (27). The experiments in Fig. 3*A* were done
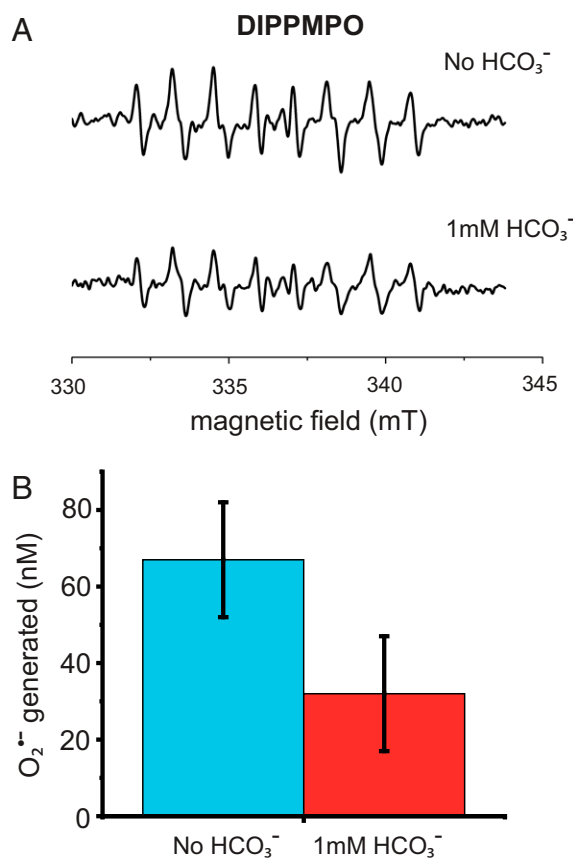

Fig. 3. EPR characterization of ROS. (*A*) Generation of $O_2^{\bullet-}$ produced in the absence (*Top*) and in the presence (*Bottom*) of 10 mM bicarbonate measured by EPR using the spin probe DIPPMPO. PSII membrane fragments (600 nM PSII cores) in 40 mM MES buffer, 5 mM MgCl, pH 6.5. The sample was illuminated with 50 μM photons m^{-2} s^{-1} red light (590 nm longpass filter) for 20 min. (*B*) $O_2^{\bullet-}$ quantified as reduced cyt c in the absence (blue bar) and in the presence (red bar) of 1 mM bicarbonate. A total of 40 to 50% $Q_A^{\bullet-}$ was obtained after three saturating flashes of a degassed sample of PSII membrane fragments (60 nM PSII cores) in the presence of 250 μM hydroxylamine in a 40 mM MES buffer, 5 mM MgCl, pH 6.5.

in the presence of catalase, which removes peroxide (formed by dismutation of the $O_2^{\bullet-}$), which could give rise to OH$^{\bullet}$ by Fenton chemistry. The presence of residual OH$^{\bullet}$ forms a spectroscopically distinct adduct with DIPPMPO (28); it can be deconvoluted from the $O_2^{\bullet-}$ be spin adduct and quantified as being less than 20% of the OH$^{\bullet}$ adduct (*SI Appendix*, Figs. S9 and S10 EPR deconvolution).

Fig. 3*A* shows that the concentration of $O_2^{\bullet-}$ formed under these conditions was diminished by $\sim$30% when the experiment was done in the presence of 12 mM bicarbonate. The higher bicarbonate concentration was used to maintain the bicarbonate ratio to PSII in the EPR experiment, in which 12 times more PSII is required to obtain appropriate signal to noise.

The spin-trapping EPR experiment showing the formation of $O_2^{\bullet-}$ was insufficiently sensitive to allow its exact quantification. A more sensitive approach is to monitor the reduction of cytochrome c (cyt c) by $O_2^{\bullet-}$ by its absorption change at 550 nm (29). Fig. 3*B* shows the amount of reduced cyt c from the reaction of $Q_A^{\bullet-}$ with O_2, in a sample containing 60 nM PSII. The sample was treated as described for the fluorescence kinetics measurements (*Materials and Methods*). The experiment was performed in the presence and absence of 1 mM bicarbonate, and the amount of reduced cyt c, which is equivalent to the

amount of $O_2^{\bullet-}$ generated, was found to be 32 ± 16 nM and 68 ± 16 nM respectively. The bicarbonate-dependent decrease in the amount of reduced cyt c corresponds to ~50% of the concentration of PSII and thus approximately the same amount of $Q_A^{\bullet-}$ present prior to O_2 addition. This confirms that $Q_A^{\bullet-}$ decay upon the addition of O_2 is due to stoichiometric $O_2^{\bullet-}$ formation. Control experiments showed that the direct reduction of cyt c by PSII was negligible, consistent with previous reports (e.g., ref. 30). Interference by H_2O_2 and $OH^{\bullet}$ on the cyt c reduction was prevented by the presence of catalase (*Materials and Methods*).

The residual cyt c reduction occurring after the addition of bicarbonate does not arise from the $Q_A^{\bullet-}$ present prior to O_2 addition, as all of that is accounted for by the bicarbonate-sensitive $O_2^{\bullet-}$. Other electron transfer components have been suggested as possible reductants of O_2 forming $O_2^{\bullet-}$, including cyt b_{559} (31) and Q_BH_2 (14) as well as the PQH_2 pool (15, 32), which could be present as a residual in our low PQ preparation. Furthermore, small amounts of contaminant Photosystem I (PSI) in the PSII-enriched thylakoid membrane (BBY)-prep (*Materials and Methods*) could represent another possible source of $O_2^{\bullet-}$. While such effects would be expected to occur to a minor extent in the dark, they could also be driven by an actinic effect of the measuring flashes. Despite their weak intensity, their frequency might result in sufficient photochemistry during the time course of the experiment to account for the observed residual $O_2^{\bullet-}$-mediated cyt c reduction (*SI Appendix*, Fig. S11). This would be consistent with the observation that experiments run in the presence of DCMU show a further decrease in the amount of reduced cyt c.

$O_2^{\bullet-}$ Production When $Q_A^{\bullet-}$ Is Generated by Continuous Illumination.

The $O_2^{\bullet-}$ accumulation was also studied by cyt c reduction under constant illumination (*SI Appendix*, Fig. S12). After 2 min of illumination (50 µmol photons m^{-2} s^{-1} red light), an average of 736 ± 10 nM reduced cyt c was generated, and when 1 mM HCO_3^- was present, this was diminished by approximately half (351 ± 60 nM). This is consistent with what we observed in the single flash stoichiometric experiments. When the same experiment was done by using 20 min of illumination without HCO_3^-, an average of $2,076 \pm 10$ nM reduced cyt c was generated, while in the presence of HCO_3^-, $1,457 \pm 60$ nM reduced cyt c was formed. The effect of HCO_3^- on decreasing the formation of reduced cyt c seemed to diminish at longer illumination periods, suggesting that other routes for production of $O_2^{\bullet-}$, such as cytochrome b_{559} and PQH_2 and perhaps involving $^1O_2$, might play a role upon prolonged illumination. Furthermore, the prolonged illumination leads to an increased probability of $Q_A^{\bullet-}$ being formed that in turn favors bicarbonate dissociation even in the presence of 1 mM bicarbonate in solution (33, 34).

When the DCMU was present in the absence of added bicarbonate, 2 min of illumination resulted in hardly detectable amounts of reduced cyt c, while after 20 min of illumination, the amount was 626 ± 70 nM (*SI Appendix*, Fig. S12). These results differ from those shown in Fig. 2*B*, where DCMU was found to be less effective than bicarbonate for inhibiting the $Q_A^{\bullet-}$ reduction of O_2 in the dark. The more pronounced effect of DCMU under continuous light could result from other reactions generating reactive oxygen species (ROS), such as long-lived $Pheo_{D1}^{\bullet-}$ and/or ^3Chl-mediated $^1O_2$ formation.

Mechanism of $Q_A^{\bullet-}$ Reduction of O_2.

To probe possible molecular mechanisms of O_2 reduction, we performed quantum chemical density functional theory (DFT) calculations and hybrid quantum mechanics/molecular mechanics (QM/MM) molecular dynamics (MD) simulations to assess the electronic structure of the nonheme iron site and its reactivity with molecular oxygen (Fig. 4 and *SI Appendix*, Fig. S13). In our DFT models, we first

optimized the structure of the nonheme iron site with either HCO_3 or an O_2 ligand bound to the Fe^{2+} ion or in the absence of either ligand. The DFT models suggested that the O_2 can bind with a high affinity (~-4 kcal mol^{-1}) to the nonheme Fe^{2+}, forming a 2.4-Å covalent bond between the Fe^{2+} and the O_2. We next added an electron on Q_A and reoptimized the models. The DFT calculations suggested that the electron was localized on Q_A, forming $Q_A^{\bullet-}$ in the HCO_3-bound form and when no exchangeable ligand on the iron was modeled (Fig. 4*A*). In contrast, in the dioxygen-bound form, the electron instantly moved from $Q_A^{\bullet-}$ to O_2 during the calculations, leading to formation of an $Fe^{II} - O_2^{\bullet}$ species (Fig. 4 *B–D*). By varying the Fe-O_2 distance, we observed that the electron transfer from $Q_A^{\bullet-}$ was triggered at around 2.6 Å, when a chemical bond forms between the dioxygen and iron (*SI Appendix*, Fig. S14). The findings thus suggest that the nonheme iron catalyzes O_2 reduction/superoxide formation (Fig. 4 *B* and *D*). Our calculations also suggested that the presence of $Q_A^{\bullet-}$ led to weakening of the HCO_3 affinity for the iron due to electrostatic repulsion, in accordance with experimental evidence (33). The calculations also support that the Fe^{3+} form of the nonheme iron can still bind HCO_3, whereas both O_2 and $O_2^{\bullet-}$ favor the Fe^{2+} form (*SI Appendix*, Fig. S15).

Hybrid QM/MM MD simulations were also done to study the dynamics of the electron transfer process in more detail, including the effects of temperature (Fig. 4 *B* and *D*, *SI Appendix*, Fig. S14, *Materials and Methods*). This was done by initiating the simulations from a state in which $Q_A^{\bullet-}$ was relaxed in classical molecular dynamics (MD) simulations. The reduction of Q_A tightened the local hydrogen bonds between the plastoquinone and His214/ Phe261 relative to the neutral Q_A state, which stabilized the reduced form by further subtle conformational changes in the surrounding helices. Consistent with our results obtained from the DFT models, we found that Q_A remained reduced throughout the 2 ps QM/MM MD simulation when HCO_3^- was bound or when no exchangeable ligand on the iron was modeled. In contrast, the electron was rapidly transferred during the initial 0.2 ps to the Fe-bound O_2, forming a $Fe^{II} - O_2^{\bullet-}$ species.

To probe structural effects linked to dissociation of HCO_3^- on longer nano-to-microsecond timescales, we performed classical atomistic MD simulations of PSII embedded in a lipid membrane, with the Q_A site modeled either as oxidized or as semiquinone, $Q_A^{\bullet-}$. During the 200 ns MD simulations, we observed two water-filled tunnels, 1 and 2, that connect the stromal side of the membrane to the nonheme Fe center, while the Q_A site remained sequestered from water molecules (Fig. 4 *E–G*, *SI Appendix*, Fig. S15). In simulations without an exchangeable ligand modeled on the nonheme iron, we observed a significant increase in the hydration state of the tunnels compared to the simulations performed when the HCO_3 was bound (Fig. 4*G*). Conformational changes around Lys264 seem to regulate the accessibility of the tunnel to the nonheme iron site (Fig. 4 *E* and *F*, *SI Appendix*, Fig. S15 *A* and *B*). We note that the water-filled tunnels are large enough for dioxygen diffusion into the site. These findings fit with the model in which occupation of the binding site on the nonheme iron prevents O_2 from binding there.

Discussion

Electron Donation from $Q_A^{\bullet-}$ to O_2.

Here, we trapped the $Q_A^{\bullet-}$ state in PSII membranes with a depleted PQ pool by illuminating in the presence of low concentrations of the electron donor, NH_2OH, under anaerobic conditions. The $Q_A^{\bullet-}$ is stable in a significant fraction of centers because forward electron transfer is blocked due to Q_B being reduced or absent in the PQ-depleted PSII. In addition, $Q_A^{\bullet-}$ cannot recombine with the stable S_0 or S_1 states on the minutes timescale of the
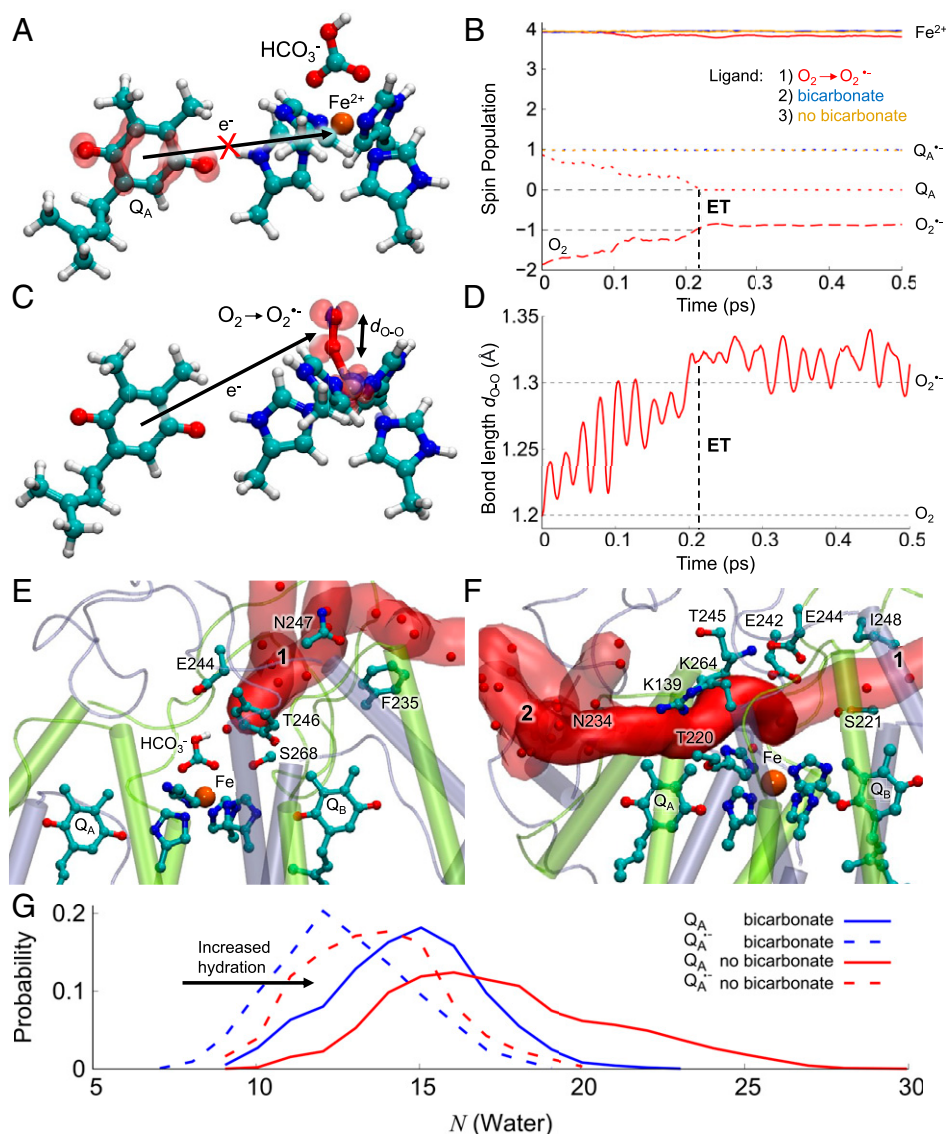
Fantuzzi et al.
Bicarbonate-controlled reduction of oxygen by the Q_A semiquinone
in Photosystem II in membranes

Fig. 4. O_2 reduction mechanism, bicarbonate binding, and accessibility of the nonheme Fe site of PSII. Structure and spin densities from DFT models of the (*A*) HCO_3^--bound and (*C*) O_2-bound forms of the nonheme iron (the state without HCO_3^- is shown in *SI Appendix*, Fig. S13*F*). The figure shows the spin density difference (red/blue sphere $\pm 0.001e$ for alpha/beta spin) after adding an electron into the system, with only the Q_A and iron/histidine residues shown for clarity (*SI Appendix*, Fig. S13). (*B*) Spin population during the QM/MM MD simulations for HCO_3^--bound (in blue) and without HCO_3^--bound (in orange) and the O_2-bound forms (in red) on the Fe^{2+} (solid lines), Q_A (dotted lines), and O_2 (dashed line). (*D*) The O-O bond length during electron transfer from Q_A. (*E* and *F*) Snapshot at 150 ns of the water-filled tunnels formed around the Q_A site during MD simulations in (*E*) with the HCO_3^--bound form and (*F*) without the HCO_3^-. (*G*) Histogram of water molecules in tunnels 1 and 2 connecting to the iron from the bulk solvent. The bicarbonate blocks water entry to the nonheme iron site.

experiment (5). The presence of $Q_A^{\bullet-}$ was monitored using chlorophyll fluorescence (17, 35). This "trapped" $Q_A^{\bullet-}$ undergoes a slow decay ($t_{1/2} = 5$ min) that may correspond to the recombination of the electron on $Q_A^{\bullet-}$ with a relatively stable oxidized species, such as $Tyr_D^{\bullet}$ (21) (Fig. 2*A*).

We used this experimental system to test if the trapped $Q_A^{\bullet-}$ would react with added O_2. Upon addition of O_2, the lifetime of the trapped $Q_A^{\bullet-}$ was found to decrease, with the reaction rate increasing with increased O_2 concentration and saturating above ~150 μM O_2 (*SI Appendix*, Fig. S3). The kinetics of the O_2-induced $Q_A^{\bullet-}$ decay showed a single exponential curve, consistent with a pseudo first-order reaction at a fixed $Q_A^{\bullet-}$ concentration, with a transition to a zero-order reaction above 150 μM O_2, thus resulting in a half-time of ~10 s under physiological O_2 concentrations (270 μM) (Fig. 2*B*).

The reaction rate did not appear to be affected by the thermodynamic driving force, as judged by the lack of effect of the phenolic herbicide, bromoxynil, which is known to lower the E_m of the $Q_A/Q_A^{\bullet-}$ redox couple (24) (Fig. 2*C* and *SI Appendix*, Fig. S4 Tyr_D $Q_A^{\bullet-}$ recomb). DCMU binding is expected to increase the E_m of the $Q_A/Q_A^{\bullet-}$ couple and thus potentially slow down the O_2 reduction. However, DCMU binding strongly inhibited the electron transfer from $Q_A^{\bullet-}$ to O_2 (Fig. 2*C*). The DCMU inhibition was so significant that it seems unlikely to result from the predicted +50 mV change in reduction potential. Possible explanations for the DCMU-induced inhibition of O_2 reduction by $Q_A^{\bullet-}$ include minor structural/conformational effects, redox effects on the nonheme iron, which may affect bicarbonate binding (see *The Nonheme Iron as the Binding Site for O_2*).

Bicarbonate and Formate Inhibition of O_2 Reduction. Under the conditions of the fluorescence measurements, the bicarbonate was expected to be depleted from its binding site on the non-heme Fe^{2+} because 1) the degassing of the sample to make it anaerobic is expected to lower the concentration of CO_2 and thus of the bicarbonate; and 2) the presence of $Q_A^{\bullet-}$ greatly decreases the affinity of the bicarbonate for its binding site on the nonheme iron (33). Therefore, we tested the effect of adding back bicarbonate prior to the addition of O_2. Bicarbonate readdition is expected to lower the E_m of $Q_A/Q_A^{\bullet-}$ and thus to increase the driving force for O_2 reduction. Instead, we found that bicarbonate addition completely blocked electron transfer from $Q_A^{\bullet-}$ to O_2 (Fig. 2D). This finding suggests that O_2 reduction occurs when it is bound to the nonheme iron in the empty bicarbonate site.

Formate had the same effect as bicarbonate. This lack of formate/bicarbonate specificity contrasts with the specific roles of bicarbonate in optimizing proton-coupled electron transfer (26, 34, 36) and in redox tuning for regulation and photoprotection (33), roles that are not shared by formate. This lack of specificity of bicarbonate-versus-formate binding is consistent with the inhibition of O_2 reduction being a steric effect, with either bicarbonate or formate binding occluding the O_2 binding site on the nonheme iron. The occlusion of the nonheme iron binding site by bicarbonate was also indicated by the MD simulations.

Formation of Superoxide. EPR spin trapping and cyt c reduction confirmed that $O_2^{\bullet-}$ was the product of the reaction of $Q_A^{\bullet-}$ with O_2 (Fig. 3) and that this reaction was blocked by bicarbonate addition. The cytochrome reduction method allowed the $O_2^{\bullet-}$ to be quantified, and its concentration was found to be close to that of the $Q_A^{\bullet-}$. A second fraction of $O_2^{\bullet-}$ was formed in the dark in a reaction that was not inhibited by bicarbonate addition and was unrelated to the oxygen-dependent decay of $Q_A^{\bullet-}$. We have not characterized the electron source of this fraction of $O_2^{\bullet-}$ formation, but we note that there are several possible candidates, including PQH_2 bound to PSII or in the membrane, cyt b_{559}, and PSI (14, 15, 31, 32).

Physiological Significance: Rates and Conditions. (In *Redox and Mechanistic Considerations*, we discuss the possibility of faster rates of O_2 reduction by $Q_A^{\bullet-}$, but in this section, we discuss the slower rate measured using the experimental approach used here.) The rate of electron transfer from $Q_A^{\bullet-}$ to O_2 ($t_{1/2} \sim 10$ s) implies that under conditions where the Q_B and quinone pool are oxidized, the reduction of O_2 is too slow to compete with the forward electron transfer rate of $t_{1/2} \sim 1$ ms (35) even when bicarbonate is absent (34). When the quinone pool is fully reduced, a large proportion of $S_2Q_A^{\bullet-}$ and $S_3Q_A^{\bullet-}$ will recombine with a $t_{1/2} \sim 1.5$ s (20), i.e., much faster than the rate of electron transfer of the $Q_A^{\bullet-}$ to O_2 reaction reported here. However, when forward electron transfer from $Q_A^{\bullet-}$ is blocked in centers where either S_1 or S_0 are present, the reaction with O_2 could be the dominant $Q_A^{\bullet-}$ reoxidation pathway, provided the bicarbonate is absent from its binding site on the nonheme iron. Such conditions are likely to occur when CO_2 levels are limiting, as previously discussed (33).

Physiological conditions other than those where the PQ pool is reduced are likely to exist in which electrons are trapped on $Q_A^{\bullet-}$ long enough to allow bicarbonate release and reduction of O_2 to be a relevant reaction. These circumstances could include those associated with assembly and photoactivation of PSII, photoinhibition, and repair, in which $Q_A^{\bullet-}$ is longer lived (9, 37–39). An intermediate state in PSII assembly is structurally modified by the binding of assembly factors (Psb27, Psb28, and Psb34) that cause the bicarbonate site on the nonheme iron to be occupied instead by a glutamate (39). This iron coordination mirrors the situation that exists in the purple bacterial reaction centers. From the present results, we expect such assembly intermediates of PSII to be unable to reduce O_2 from $Q_A^{\bullet-}$. As the Q_B site is significantly modified in this assembly intermediate, it seems likely that $Q_A^{\bullet-}$ will recombine with $Tyr_Z^{\bullet}(H^+)$ via a direct tunneling step between P^+ and $Q_A^{\bullet-}$, given the high potential of the $Q_A/Q_A^{\bullet-}$ couple prior to photo-assembly of the Mn_4CaO_5 cluster (9, 39).

The Nonheme Iron as the Binding Site for O_2. The single saturable site for O_2 reduction and its complete inhibition by bicarbonate indicate that the nonheme Fe^{2+} is the O_2 binding and reduction site. DFT and QM/MM calculations reported here further support this assignment. Our calculations showed that reduction of O_2 by $Q_A^{\bullet-}$ is favorable when oxygen binds to the Fe^{2+} in the absence of bicarbonate binding to that site. This result contrasts with a previously proposed mechanism involving direct oxidation of $Q_A^{\bullet-}$ by O_2 (12–14), which is expected to require close contact between the oxygen and the semiquinone (40). The crystal structure (41) and the MD simulations indicate that this is unlikely because the Q_A is not exposed to the solvent.

In enzymes, transition metals and Fe^{2+} in particular often activate O_2 for reduction, overcoming the intrinsic spin-transition that makes O_2, a ground state triplet, anomalously stable. It seems that this is also the case in PSII. This mechanism seems reasonable given that bicarbonate dissociates from the iron when $Q_A^{\bullet-}$ is long-lived (33).

The DCMU inhibition of O_2 reduction may also be taken as an indication that the nonheme Fe^{2+} is the O_2 binding site. DCMU binding shifts the redox potential of the Fe^{3+}/Fe^{2+} couple 120 mV to higher values, while other herbicides/inhibitors (atrazine and o-phenanthroline) induced much smaller shifts (42–44). Whether the DCMU inhibition of O_2 reduction reflects a perturbation of the electronic structure of the Fe^{2+} (as manifest by the redox shift), minor structural changes, or both of these is unclear. These effects could be responsible for DCMU inhibiting bicarbonate binding and dissociation (45, 46). Given the conditions of our experiment, it is possible that DCMU binding prevents bicarbonate loss, leaving the nonheme Fe^{2+} site occupied. This would explain the lack of O_2 reduction (Fig. 2). The observation that addition of bicarbonate to a DCMU-treated sample eliminates the residual O_2 reduction (*SI Appendix*, Fig. S10) is consistent with bicarbonate depletion is very limited when DCMU is present.

The suggestion that the nonheme Fe^{2+} could play an oxygen reduction role was already discussed (47), although superoxide was suggested to bind to the Fe^{2+}, and then to undergo further reduction to form $OH^{\bullet}$. In this mechanism, the superoxide was suggested to arise from oxygen reduction by $Q_A^{\bullet-}$ directly, a reaction that seems unlikely based on the present work. The direct catalytic role for the nonheme iron in oxygen reduction and its control by the bicarbonate, reported here, have not been discussed previously, as far as we are aware.

Redox and Mechanistic Considerations. Nominally, the electron transfer from $Q_A^{\bullet-}$ to O_2 is thermodynamically unfavorable, based on the E_m of $Q_A/Q_A^{\bullet-} = -144$ mV, a value that is shifted to -70 mV in the absence of bicarbonate (33), and thus, it is more oxidizing than $E_m = -160$ mV for $O_2/O_2^{\bullet}$ (48). However, given the very low concentration of $O_2^{\bullet-}$ compared to O_2, its functional potential is likely to be closer to ~0 mV (13), rendering the overall process thermodynamically favorable. In addition, it seems likely that the binding of the O_2 to the iron will change the redox potential of the $O_2/O_2^{\bullet-}$ couple.

Given the thermodynamic driving force and the ~8 Å distance between $Q_A^{\bullet-}$ and O_2, rapid ($\sim$ps) reaction rates are expected, as indeed observed in the QM/MM MD simulation, when O_2 was already bound to the iron. The measured reaction rates are, however, much slower ($t_{1/2} \sim10$ s), and this could be

6 of 10 | **PNAS**
https://doi.org/10.1073/pnas.2116063119

Fantuzzi et al.
Bicarbonate-controlled reduction of oxygen by the Q_A semiquinone in Photosystem II in membranes

due to the reaction rates being limited by O_2 diffusion along the constricted channels to the iron binding site (Fig. 4 *E* and *F* and *SI Appendix*, Fig. S14). This diffusional restriction could limit the measured rate in the experiments performed, i.e., when an anaerobic sample is mixed with oxygenated buffer. The possibility arises that under aerobic conditions, O_2 may be already within the access channel and thus have more rapid access to the nonheme iron. This raises the possibility that in vivo the reduction of O_2 by $Q_A^{\bullet-}$ could be faster than reported here.

The Fe^{3+}/Fe^{2+} couple has an E_m of +430 mV at this pH (44). The Fe^{2+} is located between the quinones Q_A and Q_B, but there is no evidence of a distinct redox role of the metal in the electron transfer process between the two quinones (49). Similarly, while the DFT and QM/MM calculations indicate that both Fe^{3+} and Fe^{2+} are stable with HCO_3^- bound, no Fe^{3+} is formed during the electron transfer process with O_2 bound, suggesting that the Fe^{2+} has a catalytic rather than redox role in enabling the electron transfer to O_2 (Fig. 4 and *SI Appendix*, Fig. S14).

Bicarbonate Regulatory Mechanism. Recently, it was shown that the dissociation of bicarbonate leads to an increase in the reduction potential of $Q_A/Q_A^{\bullet-}$, and consequently, the presence of $Q_A^{\bullet-}$ decreased the bicarbonate affinity for its binding site on the nonheme iron (33). The redox-tuning/bicarbonate-binding relationship suggested the following photoregulation/protection model: 1) when the intracellular CO_2 concentration is low and PSII is exposed to light, limitations in CO_2 fixation result in the overreduction of the electron transfer chain, leading to the formation of a long-lived $Q_A^{\bullet-}$; 2) the long-lived $Q_A^{\bullet-}$ triggers the dissociation of the bicarbonate by lowering its affinity for the nonheme iron; 3) the loss of the bicarbonate raises the E_m of $Q_A/Q_A^{\bullet-}$, increasing the energy gap between the $Q_A/Q_A^{\bullet-}$ and $Pheo_{D1}/Pheo_{D1}^{\bullet-}$ redox couples (33); 4) this increased energy gap disfavors the back-reaction, preventing the formation of $P^{+\bullet}Pheo^{\bullet-}$, the precursor of the chlorophyll triplet state (7) that reacts with O_2 to form damaging $^1O_2$ (9).

Our current findings that $Q_A^{\bullet-}$ can reduce O_2 and that bicarbonate binding prevents this reaction suggest another layer of complexity on the regulatory and protective role of bicarbonate in PSII (Fig. 5). Under normal functional conditions (light, high intracellular CO_2, stomata open), the $Q_A^{\bullet-}$ lifetime is expected to be short, the bicarbonate is bound, and $O_2^{\bullet-}$ formation is blocked (Fig. 5*A*), leading to minimal electron leaks. However, when the intracellular CO_2 concentration is low, the electron transfer chain is reduced, and long-lived $Q_A^{\bullet-}$ is formed, which favors bicarbonate release (Fig. 5*B*). Under these conditions, O_2 can bind to the Fe^{2+} and then be reduced by $Q_A^{\bullet-}$, forming Q_A and $O_2^{\bullet-}$ (Fig. 5*C*), which is then released (Fig. 5*D*).

The slow rate ($t_{1/2}$ = 10 s) for reoxidation of $Q_A^{\bullet-}$ will only have small effects on relieving the electron transfer block. It is debatable whether this will constitute a significant benefit to the system. As mentioned previously, this slow rate appears to represent the diffusional limit when O_2 is added to a fully anaerobic system, and it seems quite possible that faster rates may occur in equilibrated aerobic conditions. The possibility of faster O_2 reduction notwithstanding, low concentrations of superoxide can act as a signal, either directly or by dismutation to form hydrogen peroxide (11, 50, 51). Superoxide formation is stoichiometric and could accumulate, and a signaling role does not necessarily require a high concentration. PSI is usually considered the major source of superoxide (11, 15, 50). However, the different locations of the two photosystems in the thylakoid membrane and the specific localization of superoxide dismutases near PSI could allow $O_2^{\bullet-}$ produced by PSII to play a role in regulation.

Relevance to Previous Studies. The phosphorylation of the D1 protein in PSII, which is associated with the migration of damaged PSII from the grana to the stroma lamellae during PSII
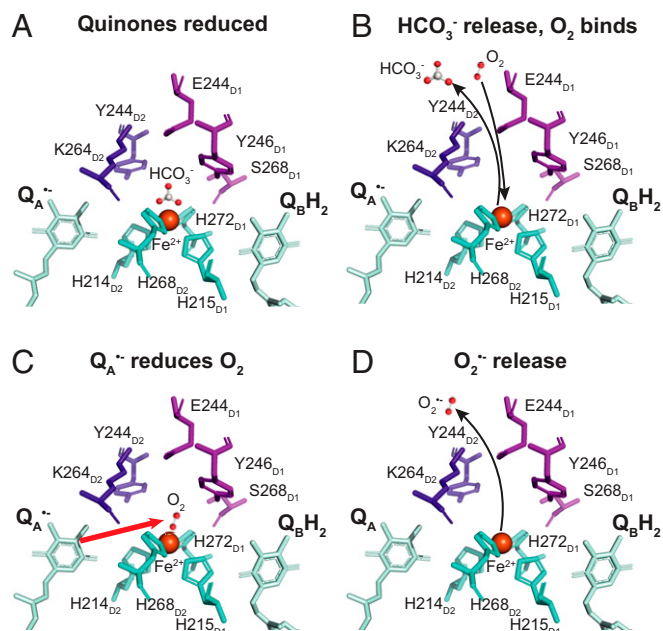

Fig. 5. Structural scheme showing the working model for O_2 reduction by $Q_A^{\bullet-}$ in PSII. (*A*) When photosynthesis is limited by low CO_2, illumination results in the reduction of the PQ pool, Q_B and Q_A. (*B*) The presence of long-lived $Q_A^{\bullet-}$ changes the dissociation constant of the bicarbonate ligand on the nonheme Fe^{2+}, leading to its release and allowing O_2 to enter the channel and to bind to the Fe^{2+}. (*C*) When the O_2 is bound to the Fe^{2+}, it is rapidly reduced by the electron coming from $Q_A^{\bullet-}$. (*D*) The superoxide formed is released from the Fe^{2+} and diffuses away.

repair cycle, was shown to decrease $O_2^{\bullet-}$ production (52). This was confirmed in STN8 kinase knockout mutant strains in rice that showed enhanced $O_2^{\bullet-}$ production under high light (53). In both cases, it was suggested that a conformational change induced by the phosphorylation (or the lack of it in the absence of the kinase in the knockout mutant) was responsible for the formation of $O_2^{\bullet-}$ due to the reduction of oxygen by $Q_B^{\bullet-}$. Considering 1) that the experiments in ref. 52 were performed in high light, 2) the improved understanding of the redox properties of Q_B (4), and 3) the findings in the present work, it seems more likely that $Q_A^{\bullet-}$ is responsible for the oxygen reduction and that the phosphorylation restricts O_2 accessibility to the nonheme iron, perhaps by favoring bicarbonate binding.

PsbS knockout mutants in rice were shown to produce more $O_2^{\bullet-}$ due to a proposed decrease in the $Q_A/Q_A^{\bullet-}$ reduction potential compared to the wild type under high light conditions (54). More recently, while investigating the role of PsbS on the efficiency of water use in field crops, a correlation between stomatal conductance and the Q_A redox state was reported (55). As hydrogen peroxide is a signal involved in stomatal opening, and as superoxide rapidly dismutates forming hydrogen peroxide, it is possible that the superoxide generated by $Q_A^{\bullet-}$ reported here contributes to this signaling pathway.

Small carboxylic acids, such as acetate and glycolate, can replace bicarbonate at the nonheme iron binding site in vivo (56, 57) and could thereby protect against photooxidative stress under low-CO_2 conditions (33, 56, 57). The mechanism involves redox tuning of Q_A and the associated binding effects of bicarbonate (33). The observation here (*SI Appendix*, Fig. S7*B*) that formate can replace bicarbonate in blocking oxygen access to the iron and thus to reduction by $Q_A^{\bullet-}$ extends this model suggesting a potential role for carboxylic acids in controlling superoxide-initiated signaling.

Fantuzzi et al.
Bicarbonate-controlled reduction of oxygen by the Q_A semiquinone in Photosystem II in membranes

PNAS | 7 of 10
https://doi.org/10.1073/pnas.2116063119

Materials and Methods

Isolation of the PSII Complex. Market spinach (*Spinacia oleracea*) was used for the isolation of PSII-enriched thylakoid membranes (BBY). Samples were prepared following the protocol from ref. 24, obtaining samples with a lower content of Q_B. To obtain samples with a lower Q_B content, preparation was the same, but samples were additionally treated with Triton X-100 at a concentration of 2.5% per milligram chlorophyll and for an incubation period of 50 min.

$Q_A^{\bullet-}$ Reoxidation Using Fluorometry. All fluorescence measurements were recorded using a Fluorometer FL3000 (Photon Systems Instruments) and carried out in the dark. For the kinetic measurements, the samples were prepared in a septum sealed cuvette. Final concentrations were 60 nM PSII and 250 μM hydroxylamine in working buffer (40 mM of 2-(*N*-morpholino)ethanesulfonic acid [MES] and 15 mM of MgCl$_2$ pH 6.5). A dark-adaptation period was set to 15 min, during which the samples were mixed and oxygen was removed by flushing with argon. $Q_A^{\bullet-}$ was trapped in 40 to 50% of centers by three saturating flashes spaced by 120 s at room temperature. Fluorescence was monitored from submilliseconds to 100 s after each flash. Oxygen was readded to the system with a gas-tight syringe by adding oxygenated buffer to the degassed samples in different proportions. The ratio of oxygenated to degassed buffer was such that the final concentration of oxygen in the sample ranged from 30 to 230 μM. Final O$_2$ concentrations, upon each addition, were monitored using the Ocean Optics Neofox Phase oxygen sensor. In the cases where oxygenated buffer was added without bicarbonate, the buffer was bubbled with air passed through Ca(OH)$_2$ to remove any HCO$_3^-$ dissolved in the buffer due to the equilibrium of the atmospheric CO$_2$ (58). When necessary, 1 mM bicarbonate, 10 μM DCMU, or 100 μM bromoxymil was added to the PSII samples prior to the degassing step. Further experimental details are provided in *SI Appendix*.

ROS Formation from O$_2$ Reacting with a Fixed Stable Amount of $Q_A^{\bullet-}$ Using cyt *c* Reduction. Reduction of cyt *c* was used to quantify the concentration of O$_2^{\bullet-}$ generated based on known concentrations of $Q_A^{\bullet-}$ and O$_2$. A fixed amount of $Q_A^{\bullet-}$ was generated following the protocol previously described for the fluorescence measurements: anaerobic, 250 μM hydroxylamine, three saturating flashes, resulting in the formation of 40 to 50% $Q_A^{\bullet-}$ being stably trapped. The experiment was initiated by the addition of oxygenated buffer corresponding to a specific final concentration of O$_2$, and after 2 min, the concentration of reduced cyt *c* was determined. The experiment was performed in the presence and in the absence of 1 mM bicarbonate using 60 nM PSII samples with 250 μM hydroxylamine in 40 mM MES and 15 mM MgCl$_2$ pH 6.5 with additional 20 μM cyt *c* and 500 U mL^{-1} catalase. Catalase was added to remove any H$_2$O$_2$ generated by spontaneous dismutation of O$_2^{\bullet-}$, which could oxidize cyt *c* by diminishing the signal. The samples containing HCO$_3^-$ were treated in the same way as for the fluorescence studies. The cyt *c* absorbance spectrum was measured using a Shimadzu UV-1601PC UV-Visible spectrophotometer, and the absorbance peak at 550 nm was used to determine the concentration of reduced cyt *c*. *SI Appendix* provides details on the ROS formation studied under continuous light conditions using cyt *c* reduction.

O$_2^{\bullet-}$ Formation Studied Using EPR. O$_2^{\bullet-}$ was trapped using DIPPMPO and spectra measured with Magnettech Miniscope MS5000. The 50-μL capillary tubes contained 60 μg mL^{-1} PSII, 10 mM DIPPMPO (28), 500 U mL^{-1} catalase, and 12 mM bicarbonate. Samples were illuminated for 2, 10, and 20 min using 50 μmol photons m^{-2} s^{-1} of red light (590 nm longpass filter) prior to measuring spectra. PSII in working buffer had HCO$_3^-$ removed when necessary by either bubbling with dry N$_2$ or with air through Ca(OH)$_2$ (58). Catalase and DIPPMPO were added after HCO$_3^-$ removal from the buffer. Spectra were measured at room temperature with 9.2-GHz microwave frequency, 100-kHz modulation frequency, 2-Gauss modulation amplitude, 3,363-Gauss field center, 150-Gauss sweep width, 3-mW microwave power, and 60-s sweep-time (59). Methylene blue was used to artificially generate ^{1}O$_2$ to establish that there was no interference between ^{1}O$_2$ generated and DIPPMPO.

Molecular Simulations. All simulations were based on the 1.9-Å resolution crystal structure of PSII from *Thermosynechococcus vulcanus* (PDB ID: 3WU2) (41), which provided a better resolved Q_A/nonheme iron site compared to the cryoEM structure of *S. oleracea* (PDB ID:3JCU) (60). The plant and cyanobacterial structures are highly similar around the region studied, and the results obtained are thus likely to apply for both systems (*SI Appendix*, Fig. S16). The crystal structure of PSII from *T. vulcanus* (PDB ID: 3WU2) (41) was embedded in a 1-palmitoyl-2-oleoyl-*sn*-glycero-3-phosphocholine membrane and solvated with TIP3P water molecules and 100 mM NaCl concentration. The total system comprised *ca.* 425,000 atoms. Parameters for all cofactors were derived from in-house DFT calculations (cf. refs. 61–63), and the remaining system was treated using the CHARMM36 force field (64). Four independent MD simulations, 200 ns each, were carried out with the Q_A site modeled either in the oxidized or anionic semiquinone ($Q_A^{\bullet-}$) state, and the nonheme iron center modeled with HCO$_3^-$-bound or without the HCO$_3^-$. The MD simulations were performed in an *NPT* ensemble at $T = 300$ K and $P = 1$ atmosphere and using a 1 fs integration timestep. Long-range electrostatics was treated using the particle mesh Ewald method. The system was gradually relaxed for 4 ns with harmonic restraints of 1 kcal mol^{-1} Å^{-1}, followed by 20-ns equilibration without restraints, and the 200-sns production runs. All classical MD simulations were performed using NAMD2 (65), and simulations were analyzed using VMD (66). Tunnels leading to the nonheme Fe site were analyzed using CAVER (67).

DFT Active Site Models and QM/MM Calculations. DFT models comprising the nonheme Fe^{2+}, its four coordinating histidine residues (His215^{D1}, His272^{D1}, His214^{D2}, His268^{D2}), the Q_A plastoquinone, Glu244^{D1}, Tyr246^{D1}, Ser268^{D1}, Glu242^{D2}, Tyr244^{D2}, and Lys264^{D2} in addition to three crystal water molecules and the CO$_3^{2-}$/HCO$_3^-$/O$_2$ ligand were built based on the crystal structure of PSII (PDB ID: 3WU2) (41). The Fe^{2+} iron was modeled in its high spin state, and anti-ferromagnetically coupled to O$_2$ using the broken symmetry DFT approach. The quantum chemical models comprised around 160 atoms. Protein residues were cut between C$_\beta$ and C$_\alpha$ atoms, except for glutamate and lysine residues, which were cut at the C$_\gamma$ and C$_\beta$ bond. Terminal carbon atoms were saturated by hydrogen atoms and kept fixed during geometry optimizations at the B3LYP-D3/def2-SVP/def2-TZVP (Fe)/$\varepsilon = 4$ level (68–70). A polarizable dielectric medium using the COSMO (71) was used to model solvation effects. Single point calculations were performed at the B3LYP-D3/def2-TZVP/ $\varepsilon = 4$ level as well as by using with B3LYP* (72), CAM-B3LYP (73), CAMh-B3LYP (74), and BHLYP (68) functionals. All calculations were performed using TURBOMOLE v. 7.2/v. 7.5 (75) and the electronic structure was visualized using VMD (66). Hybrid QM/MM calculations were performed based on the MD relaxed crystal structure of PSII (*Molecular Simulations*). The QM region was defined as in the DFT models but by additionally including the backbone of Ala260^{D2} and Phe261^{D2} to provide stabilization of the semiquinone at the Q_A site. Link atoms were introduced between C$_\alpha$ and C$_\beta$ atoms, and the QM/MM systems were relaxed using an adopted basis Newton-Raphson optimizer, followed by QM/MM dynamics at $T = 310$ K using a 1-fs integration time step. A 12-Å sphere around the QM region was allowed to relax during the QM/MM simulations. The QM/MM calculations were initiated from the $Q_A^{\bullet-}$ state with an HCO$_3^-$ or O$_2$ bound to the nonheme Fe site. All QM/MM calculations were performed using an in-house version of the CHARMM/TURBOMOLE interface (76).

Data Availability. All study data are included in the article and/or *SI Appendix*.

1. F. Rappaport, B. Diner, Primary photochemistry and energetics leading to the oxidation of the (Mn)4Ca cluster and to the evolution of molecular oxygen in Photosystem II. *Coord. Chem. Rev.* **252**, 259–272 (2008).

2. H. Dau, I. Zaharieva, Principles, efficiency, and blueprint character of solar-energy conversion in photosynthetic water oxidation. *Acc. Chem. Res.* **42**, 1861–1870 (2009).

3. T. Cardona, A. Sedoud, N. Cox, A. W. Rutherford, Charge separation in photosystem II: A comparative and evolutionary overview. *Biochim. Biophys. Acta* **1817**, 26–43 (2012).

4. S. De Causmaecker, J. S. Douglass, A. Fantuzzi, W. Nitschke, A. W. Rutherford, Energetics of the exchangeable quinone, Q$_B$, in Photosystem II. *Proc. Natl. Acad. Sci. U.S.A.* **116**, 19458–19463 (2019).

5. A. W. Rutherford, A. R. Crofts, Y. Inoue, Thermoluminescence as a probe of Photosystem II photochemistry. The origin of the flash-induced glow peaks. *Biochim. Biophys. Acta Bioenerg.* **682**, 457–465 (1982).

6. H. J. Van Gorkom, Electron transfer in photosystem II. *Photosynth. Res.* **6**, 97–112 (1985).

7. A. W. Rutherford, D. R. Paterson, J. E. Mullet, A light-induced spin-polarized triplet detected by EPR in photosystem II reaction centers. *Biochim. Biophys. Acta* **635**, 205–214 (1981).

8. N. Keren, A. Berg, P. J. van Kan, H. Levanon, I. Ohad, Mechanism of Photosystem II photoinactivation and D1 protein degradation at low light: The role of back electron flow. *Proc. Natl. Acad. Sci. U.S.A.* **94**, 1579–1584 (1997).

Fantuzzi et al.
Bicarbonate-controlled reduction of oxygen by the Q$_A$ semiquinone
in Photosystem II in membranes

9. G. N. Johnson, A. W. Rutherford, A. Krieger, A change in the midpoint potential of the quinone QA in Photosystem II associated with photoactivation of oxygen evolution. *Biochim. Biophys. Acta Bioenerg.* **1229**, 202–207 (1995).

10. A. W. Rutherford, A. Osyczka, F. Rappaport, Back-reactions, short-circuits, leaks and other energy wasteful reactions in biological electron transfer: Redox tuning to survive life in O(2). *FEBS Lett.* **586**, 603–616 (2012).

11. K.-J. Dietz, I. Turkan, A. Krieger-Liszkay, Redox- and reactive oxygen species-dependent signaling into and out of the photosynthesizing chloroplast. *Plant Physiol.* **171**, 1541–1550 (2016).

12. R. E. Cleland, S. C. Grace, Voltammetric detection of superoxide production by photosystem I. *FEBS Lett.* **457**, 348–352 (1999).

13. P. Pospíšil, Production of reactive oxygen species by photosystem II. *Biochim. Biophys. Acta* **1787**, 1151–1160 (2009).

14. P. Pospíšil, Production of reactive oxygen species by photosystem II as a response to light and temperature stress. *Front. Plant Sci.* **7**, 1950 (2016).

15. M. A. Kozuleva, B. N. Ivanov, D. V. Vetoshkina, M. M. Borisova-Mubarakshina, Minimizing an electron flow to molecular oxygen in photosynthetic electron transfer chain: An evolutionary view. *Front. Plant Sci.* **11**, 211 (2020).

16. L. K. Frankel, L. Sallans, P. A. Limbach, T. M. Bricker, Oxidized amino acid residues in the vicinity of Q(A) and Pheo(D1) of the photosystem II reaction center: Putative generation sites of reducing-side reactive oxygen species. *PLoS One* **8**, e58042 (2013).

17. A. R. Crofts, C. A. Wraight, The electrochemical domain of photosynthesis. *Biochim. Biophys. Acta Bioenerg.* **726**, 149–185 (1983).

18. I. Vass, D. Kirilovsky, A.-L. Etienne, UV-B radiation-induced donor- and acceptor-side modifications of photosystem II in the cyanobacterium *Synechocystis* sp. PCC 6803. *Biochemistry* **38**, 12786–12794 (1999).

19. R. D. Guiles *et al.*, The S0 state of photosystem II induced by hydroxylamine: Differences between the structure of the manganese complex in the S0 and S1 states determined by X-ray absorption spectroscopy. *Biochemistry* **29**, 486–496 (1990).

20. B. Bouges-Bocquet, Limiting steps in photosystem II and water decomposition in *Chlorella* and spinach chloroplasts. *Biochim. Biophys. Acta* **292**, 772–785 (1973).

21. G. N. Johnson, A. Boussac, A. W. Rutherford, The origin of 40–50°C thermoluminescence bands in Photosystem II. *Biochim. Biophys. Acta Bioenerg.* **1184**, 85–92 (1994).

22. A. Joliot, P. Joliot, Etude cinétique de la réaction photochimique libérant l'oxygène au cours de la photosynthèse. *C.R. Acad. Sci. Paris* **258**, 4622–4625 (1964).

23. J. Lavergne, H. W. Trissl, Theory of fluorescence induction in photosystem II: Derivation of analytical expressions in a model including exciton-radical-pair equilibrium and restricted energy transfer between photosynthetic units. *Biophys. J.* **68**, 2474–2492 (1995).

24. A. Krieger-Liszkay, A. W. Rutherford, Influence of herbicide binding on the redox potential of the quinone acceptor in photosystem II: Relevance to photodamage and phytotoxicity. *Biochemistry* **37**, 17339–17344 (1998).

25. J. J. Govindjee, J. J. Eaton-Rye, Electron transfer through photosystem II acceptors: Interaction with anions. *Photosynth. Res.* **10**, 365–379 (1986).

26. A. Sedoud *et al.*, Semiquinone-iron complex of photosystem II: EPR signals assigned to the low-field edge of the ground state doublet of Q_A•-Fe^{2+} and Q_B•-Fe^{2+}. *Biochemistry* **50**, 6012–6021 (2011).

27. A. Steffen-Heins, B. Steffens, EPR spectroscopy and its use in planta—A promising technique to disentangle the origin of specific ROS. *Front. Environ. Sci.* **3**, 15 (2015).

28. K. Abbas *et al.*, Medium-throughput ESR detection of superoxide production in undetached adherent cells using cyclic nitrone spin traps. *Free Radic. Res.* **49**, 1122–1128 (2015).

29. G. Ananyev, G. Renger, U. Wacker, V. Klimov, The photoproduction of superoxide radicals and the superoxide dismutase activity of Photosystem II. The possible involvement of cytochrome b559. *Photosynth. Res.* **41**, 327–338 (1994).

30. S. Larom, F. Salama, G. Schuster, N. Adir, Engineering of an alternative electron transfer path in photosystem II. *Proc. Natl. Acad. Sci. U.S.A.* **107**, 9650–9655 (2010).

31. N. Bondarava *et al.*, Putative function of cytochrome b559 as a plastoquinol oxidase. *Physiol. Plant.* **138**, 463–473 (2010).

32. M. M. Borisova-Mubarakshina, D. V. Vetoshkina, B. N. Ivanov, Antioxidant and signaling functions of the plastoquinone pool in higher plants. *Physiol. Plant.* **166**, 181–198 (2019).

33. K. Brinkert, S. De Causmaecker, A. Krieger-Liszkay, A. Fantuzzi, A. W. Rutherford, Bicarbonate-induced redox tuning in Photosystem II for regulation and protection. *Proc. Natl. Acad. Sci. U.S.A.* **113**, 12144–12149 (2016).

34. D. Shevela, J. J. Eaton-Rye, J.-R. Shen, Govindjee, Photosystem II and the unique role of bicarbonate: A historical perspective. *Biochim. Biophys. Acta* **1817**, 1134–1151 (2012).

35. R. de Wijn, H. J. van Gorkom, Kinetics of electron transfer from Q(a) to Q(b) in photosystem II. *Biochemistry* **40**, 11912–11922 (2001).

36. N. Cox *et al.*, The semiquinone-iron complex of photosystem II: Structural insights from ESR and theoretical simulation; evidence that the native ligand to the non-heme iron is carbonate. *Biophys. J.* **97**, 2024–2033 (2009).

37. P. J. Nixon, J. T. Trost, B. A. Diner, Role of the carboxy terminus of polypeptide D1 in the assembly of a functional water-oxidizing manganese cluster in photosystem II of the cyanobacterium *Synechocystis* sp. PCC 6803: Assembly requires a free carboxyl group at C-terminal position 344. *Biochemistry* **31**, 10859–10871 (1992).

38. K. Zimmermann *et al.*, Herbicide binding and thermal stability of photosystem II isolated from *Thermosynechococcus elongatus*. *Biochim. Biophys. Acta* **1757**, 106–114 (2006).

39. J. Zabret *et al.*, Structural insights into photosystem II assembly. *Nat. Plants* **7**, 524–538 (2021).

40. J. R. T. J. Wass, E. Ahlberg, I. Panas, D. J. Schiffrin, Quantum chemical modelling of the rate determining step for oxygen reduction on quinones. *Phys. Chem. Chem. Phys.* **8**, 4189–4199 (2006).

41. Y. Umena, K. Kawakami, J.-R. Shen, N. Kamiya, Crystal structure of oxygen-evolving photosystem II at a resolution of 1.9 Å. *Nature* **473**, 55–60 (2011).

42. C. A. Wraight, Modulation of herbicide-binding by the redox state of Q400, an endogenous component of Photosystem II. *Biochim. Biophys. Acta Bioenerg.* **809**, 320–330 (1985).

43. B. A. Diner, V. Petrouleas, Light-induced oxidation of the acceptor-side Fe(II) of Photosystem II by exogenous quinones acting through the QB binding site. II. Blockage by inhibitors and their effects on the Fe(III) EPR spectra. *Biochim. Biophys. Acta Bioenerg.* **893**, 138–148 (1987).

44. B. A. Diner, V. Petrouleas, Q400, the non-heme iron of the photosystem II iron-quinone complex. A spectroscopic probe of quinone and inhibitor binding to the reaction center. *Biochim. Biophys. Acta Bioenerg.* **895**, 107–125 (1987).

45. J. F. H. Snel, J. J. S. van Rensen, Kinetics of the reactivation of the Hill reaction in CO_2-depleted chloroplasts by addition of bicarbonate in the absence and in the presence of herbicides. *Physiol. Plant.* **57**, 422–427 (1983).

46. D. J. Blubaugh, Govindjee, Comparison of bicarbonate effects on the variable chlorophyll a fluorescence of CO_2-depleted and non-CO_2-depleted thylakoids in the presence of diuron. *Z. Naturforsch. C* **39**, 378–381 (1984).

47. P. Pospíšil, A. Arató, A. Krieger-Liszkay, A. W. Rutherford, Hydroxyl radical generation by photosystem II. *Biochemistry* **43**, 6783–6792 (2004).

48. P. Wardman, Reduction potentials of one-electron couples involving free radicals in aqueous solution. *J. Phys. Chem. Ref. Data* **18**, 1637–1755 (1989).

49. P. Chernev, I. Zaharieva, H. Dau, M. Haumann, Carboxylate shifts steer interquinone electron transfer in photosynthesis. *J. Biol. Chem.* **286**, 5368–5374 (2011).

50. F.-J. Schmitt *et al.*, Reactive oxygen species: Re-evaluation of generation, monitoring and role in stress-signaling in phototrophic organisms. *Biochim. Biophys. Acta* **1837**, 835–848 (2014).

51. G. Noctor, J.-P. Reichheld, C. H. Foyer, ROS-related redox regulation and signaling in plants. *Semin. Cell Dev. Biol.* **80**, 3–12 (2018).

52. L. Chen *et al.*, Protecting effect of phosphorylation on oxidative damage of D1 protein by down-regulating the production of superoxide anion in photosystem II membranes under high light. *Photosynth. Res.* **112**, 141–148 (2012).

53. R. S. Poudyal, K. Nath, I. S. Zulfugarov, C.-H. Lee, Production of superoxide from photosystem II-light harvesting complex II supercomplex in STN8 kinase knock-out rice mutants under photoinhibitory illumination. *J. Photochem. Photobiol. B* **162**, 240–247 (2016).

54. I. S. Zulfugarov *et al.*, Production of superoxide from Photosystem II in a rice (*Oryza sativa* L.) mutant lacking PsbS. *BMC Plant Biol.* **14**, 242 (2014).

55. K. Głowacka *et al.*, Photosystem II Subunit S overexpression increases the efficiency of water use in a field-grown crop. *Nat. Commun.* **9**, 868 (2018).

56. T. Roach, A. Sedoud, A. Krieger-Liszkay, Acetate in mixotrophic growth medium affects photosystem II in *Chlamydomonas reinhardtii* and protects against photoinhibition. *Biochim. Biophys. Acta* **1827**, 1183–1190 (2013).

57. M. Messant *et al.*, Glycolate induces redox tuning of photosystem II in vivo: Study of a photorespiration mutant. *Plant Physiol.* **177**, 1277–1285 (2018).

58. S. Korshunov, J. A. Imlay, Detection and quantification of superoxide formed within the periplasm of *Escherichia coli*. *J. Bacteriol.* **188**, 6326–6334 (2006).

59. C. Fufezan, A. W. Rutherford, A. Krieger-Liszkay, Singlet oxygen production in herbicide-treated photosystem II. *FEBS Lett.* **532**, 407–410 (2002).

60. X. Wei *et al.*, Structure of spinach photosystem II-LHCII supercomplex at 3.2 Å resolution. *Nature* **534**, 69–74 (2016).

61. I. Ugur, A. W. Rutherford, V. R. I. Kaila, Redox-coupled substrate water reorganization in the active site of Photosystem II—The role of calcium in substrate water delivery. *Biochim. Biophys. Acta* **1857**, 740–748 (2016).

62. A. Boussac *et al.*, The low spin-high spin equilibrium in the S2-state of the water oxidizing enzyme. *Biochim. Biophys. Acta Bioenerg.* **1859**, 342–356 (2018).

63. C.-M. Suomivuori, N. O. C. Winter, C. Hättig, D. Sundholm, V. R. I. Kaila, Exploring the light-capturing properties of photosynthetic chlorophyll clusters using large-scale correlated calculations. *J. Chem. Theory Comput.* **12**, 2644–2651 (2016).

64. J. Huang *et al.*, CHARMM36m: An improved force field for folded and intrinsically disordered proteins. *Nat. Methods* **14**, 71–73 (2017).

65. J. C. Phillips *et al.*, Scalable molecular dynamics on CPU and GPU architectures with NAMD. *J. Chem. Phys.* **153**, 044130 (2020).

66. W. Humphrey, A. Dalke, K. Schulten, VMD: Visual molecular dynamics. *J. Mol. Graph.* **14**, 33–38, 27–28 (1996).

67. E. Chovancova *et al.*, CAVER 3.0: A tool for the analysis of transport pathways in dynamic protein structures. *PLoS Comput. Biol.* **8**, e1002708 (2012).

68. A. D. Becke, Density-functional thermochemistry. III. The role of exact exchange. *J. Chem. Phys.* **98**, 5648–5652 (1993).

69. C. Lee, W. Yang, R. G. Parr, Development of the Colle–Salvetti correlation-energy formula into a functional of the electron density. *Phys. Rev. B Condens. Matter* **37**, 785–789 (1988).

70. A. Schäfer, H. Horn, R. Ahlrichs, Fully optimized contracted Gaussian basis sets for atoms Li to Kr. *J. Chem. Phys.* **97**, 2571–2577 (1992).

BIOCHEMISTRY

BIOPHYSICS AND COMPUTATIONAL BIOLOGY

71. A. Klamt, G. Schüürmann, COSMO: A new approach to dielectric screening in solvents with explicit expressions for the screening energy and its gradient. *J. Chem. Soc., Perkin Trans.* **2**, 799–805 (1993).

72. M. Reiher, O. Salomon, B. Artur Hess, Reparameterization of hybrid functionals based on energy differences of states of different multiplicity. *Theor. Chem. Acc.* **107**, 48–55 (2001).

73. T. Yanai, D. P. Tew, N. C. Handy, A new hybrid exchange–correlation functional using the Coulomb-attenuating method (CAM-B3LYP). *Chem. Phys. Lett.* **393**, 51–57 (2004).

74. Y. Shao, Y. Mei, D. Sundholm, V. R. I. Kaila, Benchmarking the performance of time-dependent density functional theory methods on biochromophores. *J. Chem. Theory Comput.* **16**, 587–600 (2020).

75. R. Ahlrichs, M. Bär, M. Häser, H. Horn, C. Kölmel, Electronic structure calculations on workstation computers: The program system turbomole. *Chem. Phys. Lett.* **162**, 165–169 (1989).

76. S. Riahi, C. N. Rowley, The CHARMM-TURBOMOLE interface for efficient and accurate QM/MM molecular dynamics, free energies, and excited state properties. *J. Comput. Chem.* **35**, 2076–2086 (2014).

Fantuzzi et al.
Bicarbonate-controlled reduction of oxygen by the Q_A semiquinone
in Photosystem II in membranes